Numerical Analysis of Knudsen Number of Helium Flow Through Gas-Focused Liquid Sheet Micro-Nozzle

Krištof Kovačič [1] , Saša Bajt [2,3] and Božidar Šarler [1,4,*]

1 Laboratory for Fluid Dynamics and Thermodynamics, Faculty of Mechanical Engineering, University of Ljubljana, Aškerčeva 6, 1000 Ljubljana, Slovenia; kristof.kovacic@fs.uni-lj.si
2 Center for Free-Electron Laser Science CFEL, Deutsches Elektronen-Synchrotron DESY, Notkestr. 85, 22607 Hamburg, Germany; sasa.bajt@desy.de
3 The Hamburg Centre for Ultrafast Imaging, Luruper Chaussee 149, 22761 Hamburg, Germany
4 Laboratory for Simulation of Materials and Processes, Institute of Metals and Technology, Lepi pot 11, 1000 Ljubljana, Slovenia
* Correspondence: bozidar.sarler@fs.uni-lj.si

Abstract: This work aims to verify whether the continuum mechanics assumption holds for the numerical simulation of a typical sample delivery system in serial femtosecond crystallography (SFX). Knudsen numbers were calculated based on the numerical simulation results of helium flow through the gas-focused liquid sheet nozzle into the vacuum chamber, representing the upper limit of Knudsen number for such systems. The analysed flow is considered steady, compressible, and laminar. The numerical results are mesh-independent, with a Grid Convergence Index significantly lower than 1% for global and local analysis. This study is based on an improved definition of the numerical Knudsen number: a combination of the cell Knudsen number and the physical Knudsen number. In the analysis, no-slip boundary and low-pressure boundary slip conditions are compared. No significant differences are observed. This study justifies using computational fluid dynamics (CFD) analysis for SFX sample delivery systems based on the assumption of continuum mechanics.

Keywords: Knudsen number; compressible hypersonic flow; vacuum; liquid sheet nozzle; sample delivery system; CFD

1. Introduction

Serial femtosecond crystallography (SFX) [1] is a new technique that was enabled by intense, coherent, and pulsed X-ray sources called X-ray free electron lasers (XFEL). It is used to study static and dynamic structures of protein crystals. In SFX, micron-sized protein crystals are carried into an X-ray beam via very thin jets that are focused by the high-velocity gas flow. Such flow-focused jets [2], most commonly produced by gas dynamic virtual nozzles (GDVNs) [3,4], have jet diameters much smaller than Rayleigh jets. Due to the weak interaction between matter and X-rays, the diffraction of these protein crystals is rather low when the X-ray pulse hits the crystal. Signal can be increased by lowering the background scattering [5,6] coming from the water. This is achieved by reducing the jet diameter. Another way is to use helium as a focusing gas in a vacuum [4]. Sub-micron liquid sheet thickness jets can also reduce background scattering. Liquid sheets (also called flat jets) can be produced by colliding liquid jets [7–18] or by colliding gas jets with the middle liquid jet to achieve a sub-micron thickness [10,14,19–22].

Numerical simulations [23,24] have been used with experimental approaches to test the different nozzle designs for sample delivery systems. To choose the optimum microscopic nozzle size, gas compressibility and high velocity focusing gas, which flow along the microscopic jet in a vacuum, must be considered. The compressibility effects become important when the Mach number, $Ma = U/c$, a ratio of flow velocity U to the speed of sound c, is larger than 0.3. In sample delivery systems, the flow ranges from choked flow

(Ma $\approx$ 1) [25,26] to supersonic regime (1 < Ma < 5) [27], where the liquid sheet nozzle operates typically. Because of the gas expansion in the vacuum, its density is decreased, causing the mean free path of helium molecules to increase, where rarefied gas effects could become non-negligible.

A suitable gas flow formulation is characterised by the physical Knudsen number $Kn_p = \lambda/L$, a ratio of the molecular mean free path λ to a characteristic length scale L. Depending on the value of Kn_p, gas flows are classified into four regimes [28]:

- Continuum regime ($Kn_p < 0.01$): In this regime, the continuum assumption holds and the Navier–Stokes (N–S) equations with no-slip boundary conditions are used in numerical solutions.
- Slip flow regime ($0.01 < Kn_p < 0.1$): The no-slip condition at the solid wall no longer holds, resulting in a slip velocity at the boundary. Although the Navier–Stokes equations are still applicable, slip boundary conditions are implemented to account for this effect.
- Transitional regime ($0.1 < Kn_p < 10$): The continuum assumption and slip conditions start to break down.
- Free molecular regime ($Kn_p > 10$): The continuum assumption is invalid, and the continuum theory can no longer be applied.

CFD solves Navier–Stokes equations based on a continuum mechanics assumption. However, this approach can become questionable for the numerical simulations of microjets in sample delivery systems operating in a vacuum. The continuum mechanics assumption in these systems is generally justified with the evaluated integral Knudsen number based on overall global variables [24]. It was additionally shown that the cell Knudsen number should also be considered [29,30].

This study investigates the Knudsen number in detail, questioning whether the CFD approach, based on continuum mechanics assumption, is suitable for hypersonic compressible flow (Ma > 5) in sample delivery systems considered here. The Knudsen number is proportional ($Kn_p \propto Ma/Re$) to the ratio between the Mach and Reynolds number $Re = \rho U L/\mu$, which is the ratio between the gas density ρ, velocity U, characteristic length L, and dynamic viscosity μ. Both Mach and Reynolds numbers are proportional to the change in velocity if all other variables are kept constant. Therefore, when changing gas mass flow only, the Knudsen number remains constant since the ratio Ma/Re is independent of velocity U. In sample delivery systems, higher gas mass flow causes higher temperature drop. Because the speed of sound changes with temperature, the ratio Ma/Re is not constant when changing gas mass flow in these systems. However, the Knudsen number remains within the same order of magnitude because Ma/Re does not change drastically. The case investigated in this paper is simulated for helium mass flow of 20.4 mg/min (with Mach and Reynolds number Ma $\approx$ 6, Re $\approx$ 31), representing the upper limit for gas-focused liquid sheet nozzles, where typical helium mass flows around 10 mg/min is applied [20]. As explained before, the Knudsen number of the investigated case would remain of the same order of magnitude even for lower helium mass flows. In other sample delivery systems [25], the gas Knudsen numbers are lower due to the higher Reynolds numbers (up to 1200) and lower or similar Mach numbers. Thus, the presented study explores the upper limit of the expected Knudsen numbers in sample delivery systems. For the analysed gas-focused liquid sheet nozzle, estimated Knudsen numbers are 4×10^{-5} for the vacuum chamber and 4×10^{-3} inside the nozzle, approaching the transitional regime.

This paper is divided into five sections. After the introduction, we define the Knudsen number and governing equations. In the Section 3, we introduce the numerical methods and show the results of the grid convergence study. This is followed by presenting and discussing our results, where we focus on comparing results obtained with low-pressure boundary slip (LPBS) and no-slip boundary conditions. In the Section 5, we summarise our findings and conclusions.

2. Methods

2.1. Knudsen Number

Rarefied gas dynamics are characterised by the physical Knudsen number, where the free mean path λ is determined as

$$\lambda = \frac{\mu}{\rho} \sqrt{\frac{\pi m}{2 k_B T}}, \tag{1}$$

where μ is dynamic viscosity, ρ is density, m is molecular mass, k_B is the Boltzmann constant, and T temperature. As compared to the ideal gas law with $\rho = mp/(k_B T)$, Equation (1) can be rearranged to

$$\lambda = \frac{\mu}{p} \sqrt{\frac{\pi R T}{2}}, \tag{2}$$

where p is pressure and R is the specific gas constant. For compressible flows, the Knudsen number can be defined with the physical Reynolds number $\mathrm{Re_p} = \rho U L_p / \mu$ and the Mach number $\mathrm{Ma} = U/c$, where U is fluid velocity magnitude, L_p is physical characteristic length, and $c = \sqrt{\gamma R T / M}$ the speed of sound, defined by the ratio of specific heats γ, specific gas constant R, temperature T, and molar mass M. The Mach, Reynolds, and Knudsen numbers are related as

$$\mathrm{Kn_p} = \frac{\mathrm{Ma}}{\mathrm{Re_p}} \sqrt{\frac{\gamma \pi}{2}}. \tag{3}$$

In CFD, the cell Knudsen number $\mathrm{Kn_c} = \lambda / \Delta x$ is defined as the ratio between the mean free path λ to cell size Δx. Alternatively, the cell Knudsen number can be defined as

$$\mathrm{Kn_c} = \frac{\mathrm{Ma}}{\mathrm{Re_c}} \sqrt{\frac{\gamma \pi}{2}}, \tag{4}$$

where $\mathrm{Ma} = U/c$ is the local Mach number, and $\mathrm{Re_c} = \rho U \Delta x / \mu$ is a cell Reynolds number. Hence, for the well-resolved flows, where the cell size is much smaller than the physical characteristic length, the cell Knudsen number is much larger than the physical Knudsen number $\mathrm{Kn_c} \gg \mathrm{Kn_p}$, meaning that the $\mathrm{Kn_c}$ might exceed the continuum limit, while the $\mathrm{Kn_p}$ stays in continuum regime.

The numerical Knudsen number $\mathrm{Kn_n} = \lambda / L_n$, which also affects the solution, is a combination of the physical and cell Knudsen numbers, determined by a soft-minimum function [29,30]:

$$\mathrm{Kn_n} = \mathrm{softmin}(\mathrm{Kn_p}, \mathrm{Kn_c}). \tag{5}$$

In [29], softmin function was proposed as

$$\mathrm{Kn_n} = 10^{\ln(\exp(\lg(\mathrm{Kn_p})) + \exp(\lg(\mathrm{Kn_c})))}. \tag{6}$$

For well-resolved flows, the numerical Knudsen number converges to a physical Knudsen number $\mathrm{Kn_n} \to \mathrm{Kn_p}$. At the same time, for the unresolved flow where $\mathrm{Kn_c} \ll \mathrm{Kn_p}$, the numerical Knudsen number converges to the cell Knudsen number $\mathrm{Kn_n} \to \mathrm{Kn_c}$. However, Equation (6) seems to turn the limits around because the result is closer to the higher value between $\mathrm{Kn_p}$ and $\mathrm{Kn_c}$, therefore representing maximum rather than minimum, which is explained in Section 4.3. As an alternative to Equation (6), we propose

$$\mathrm{Kn_n} = -\log\left(e^{-\mathrm{Kn_p}} + e^{-\mathrm{Kn_c}}\right), \tag{7}$$

which is a combination of the softmin function and the log-exp-sum function [31–33]. Thesoftmin function is analogous to the softmax function (widely used in machine learning algorithms), while the log-exp-sum function is similar to [31].

The expression in Equation (7) has a downside for $\text{Kn}_p \approx \text{Kn}_c < 0$ because it returns a negative value, having no physical meaning. Furthermore, it can return $\text{Kn}_n < \min(\text{Kn}_p, \text{Kn}_c)$, which is also not expected since the numerical Knudsen number should lie within the interval $(\text{Kn}_p, \text{Kn}_c)$ when $\text{Kn}_p < \text{Kn}_c$ or $(\text{Kn}_c, \text{Kn}_p)$ when $\text{Kn}_c < \text{Kn}_p$. Therefore, we suggest the following condition for the numerical Knudsen number $\text{Kn}_{n,P}$ in point $P(x, y, z)$, which limits the maximum $\text{Kn}_{n,\max} = \max(\text{Kn}_p, \text{Kn}_c)$ and minimum $\text{Kn}_{n,\min} = \min(\text{Kn}_p, \text{Kn}_c)$ based on Kn_p and Kn_c:

$$\text{Kn}_{n,P} = \begin{cases} \text{Kn}_{n,\min} & \text{Kn}_{n,\min} > \text{Kn}_n \\ \text{Kn}_n & \text{Kn}_{n,\min} < \text{Kn}_n < \text{Kn}_{n,\max} \end{cases}. \tag{8}$$

2.2. Governing Equations

Let us analyse steady, laminar, compressible helium flow in vacuum conditions. The flow has been resolved in ANSYS Fluent 2023R2 using a pressure-based solver. Historically, a density-based solver has been developed for compressible flows. In this paper, we used a pressure-based solver because of the intended future calculations of two-phase flow, where the volume of fluid (VOF) and density-based solver are incompatible. However, we did not find any difference between density-based and pressure-based solvers for typical SFX conditions, a conclusion to be elaborated on in one of our future publications. The flow is described with continuity, momentum, and energy equations, respectively:

$$\nabla \cdot (\rho \boldsymbol{v}) = 0, \tag{9}$$

$$\nabla \cdot (\rho \boldsymbol{v} \boldsymbol{v}) = -\nabla p + \nabla \cdot \overline{\boldsymbol{\tau}}, \tag{10}$$

$$\nabla \cdot \left(\rho c_p T \boldsymbol{v} + \frac{1}{2} \rho |\boldsymbol{v}|^2 \boldsymbol{v} \right) = -\nabla \cdot (\boldsymbol{v} p) + \nabla \cdot (k \nabla T) + \nabla \cdot (\overline{\boldsymbol{\tau}} \boldsymbol{v}), \tag{11}$$

where $\boldsymbol{v}$ is the velocity vector, p is pressure, $\overline{\boldsymbol{\tau}}$ is viscous stress tensor, defined as $\overline{\boldsymbol{\tau}} = \mu \left[(\nabla \boldsymbol{v}) + (\nabla \boldsymbol{v})^T \right] - 2/3\, \mu (\nabla \times \boldsymbol{v}) \mathbf{I}$, where μ and $\mathbf{I}$ stand for dynamic viscosity and identity tensor, respectively. For the analysed helium flow, bulk viscosity is not included because monoatomic gases exhibit negligible bulk viscosity [32–42]. c_p is mass-specific heat at constant pressure, T is temperature, and k is thermal conductivity. Term $(\overline{\boldsymbol{\tau}} \boldsymbol{v})$ represents viscous dissipation. Density is determined by the ideal gas law $\rho = pM/RT$, and dynamic viscosity from the Sutherland law $\mu = A_S \sqrt{T}/(1 + T_S/T)$, with values for helium $A_S = 1.48 \times 10^{-6}$ kg/msK$^{1/2}$ and $T_S = 79$ K [43].

3. The Numerical Method

3.1. Spatial Discretisation

The computational fluid domain coincides with the bottom part of the gas-focused liquid sheet nozzle, shown in Figure 1a,b, where the cross-section of the extracted fluid domain is shown. Capillaries are long enough that a fully developed velocity profile is established. The computational structured mesh is hexahedral, with 6 levels of refinement regions with non-conformal transitions. The cell size of the finest level is denoted as Δx_0. The cell size of each next level is two times larger than the previous one $\Delta x_l = 2^l \Delta x_0$ (level $l \in (0.5)$). Due to the symmetrical design, only a quarter of the nozzle was analysed to reduce the computational time, as shown in Figure 1c, which shows the nozzle model and computational mesh. Three meshes, M1, M2, and M3, where M1 is the finest mesh and M3 is the coarsest, were generated in ANSYS Meshing to perform a grid independence study. The details of each mesh can be found in Table 1.
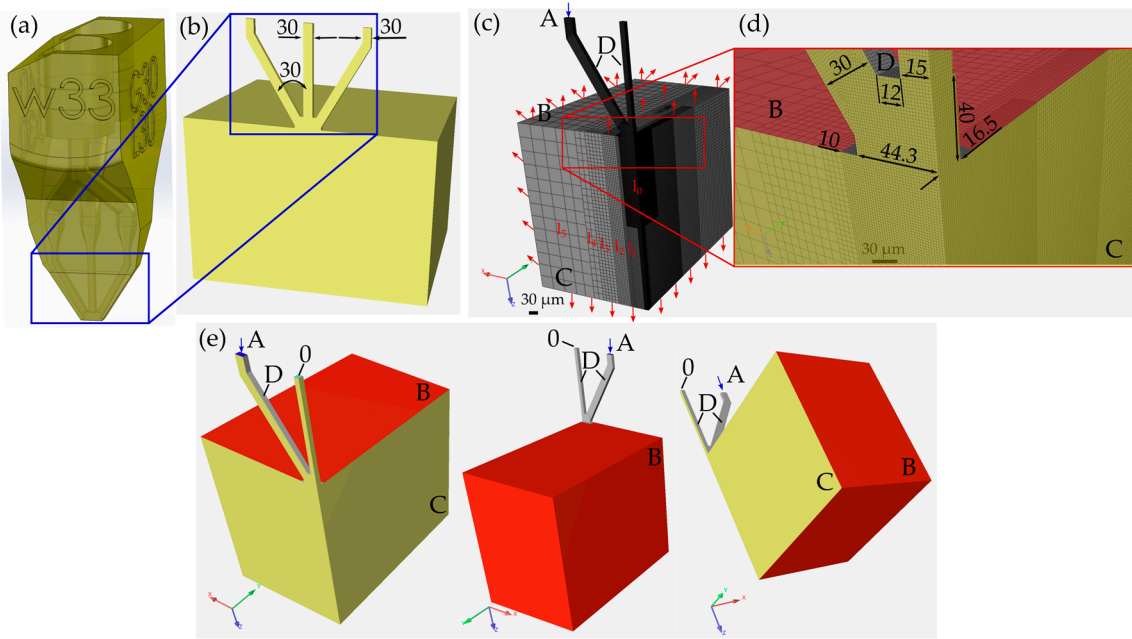
Figure 1. Fluid domain and computational grid: (**a**) liquid sheet nozzle; (**b**) fluid domain; (**c**) mesh M2; (**d**) detail of the mesh M2; (**e**) boundary conditions: A—mass flow inlet; B—pressure outlet; C—symmetry; D—walls; 0—zero velocity inlet. All dimensions are shown in μm and degrees. l_{0-5} represent the mesh level, l_0 being the finest and l_5 being the coarsest.

Table 1. Information about meshes and numerical simulations.

	M1	**M2**	**M3**
Δx_0 [μm]	0.75	1.5	2
Nr. of cells	4,426,090	547,730	234,240
Nr. of iterations	260	250	226
Residuals (continuity equation)	3×10^{-4}	1×10^{-6}	1×10^{-6}
Residuals (momentum and energy equation)	2×10^{-6}	1×10^{-9}	1×10^{-9}
Calculation time [core hours]	6.9	0.63	0.21

3.2. Boundary Conditions

The computational domain consists of four boundary patch types, i.e., mass flow inlet (1/4 of 20.4 mg/min), pressure outlet with zero-gauge pressure, symmetry, and wall (no-slip/LPBS, T = 293 K), as demonstrated in Figure 1e. The middle capillary provides liquid flow, which will be analysed in the future. Therefore, as shown in Figure 1e, a zero-velocity inlet was set at this location. The operating pressure is set to 1000 Pa.

An LPBS is used instead of the no-slip boundary condition in the slip regime. Here, the gas-phase velocity at a solid surface differs from the velocity at which the wall moves, and the gas temperature at the surface differs from the wall temperature. Due to their simplicity and effectiveness, Maxwell's models are adopted in ANSYS Fluent to describe these physical phenomena [44]. The velocity slip is defined as

$$U_w - U_g = \left(\frac{2 - \alpha_v}{\alpha_v} \right) \mathrm{Kn} L_c \frac{\partial U}{\partial n} \approx \left(\frac{2 - \alpha_v}{\alpha_v} \right) \frac{\lambda}{\delta} (U_g - U_c), \tag{12}$$

$$V_g \equiv (\boldsymbol{V} \cdot \boldsymbol{n})_g = V_w. \tag{13}$$

Here, U and V represent the velocity components that are tangential and normal to the wall, respectively. The subscripts g, w, and c indicate gas, wall, and cell-centre velocities. δ is the distance from the cell centre to the wall. L_c is the characteristic length. α_v is the

momentum accommodation coefficient of the gas mixture. Its value is calculated as the mass-fraction weighted average of each gas species in the system [44]. In our case, it equals unity. The mean free path is computed as follows:

$$\lambda = \frac{k_B T}{\sqrt{2}\pi\sigma^2 p},$$ (14)

where σ is Lennard—ones characteristic length, which equals to 260 pm for helium [45].

Equations (12) and (13) indicate that while the gas velocity component normal to the wall is the same as the normal velocity, the tangential components slip. The values lie somewhere between the cell-centre and the wall values. These two equations can be combined to give a generalised formulation [44]:

$$V_g = \frac{V_w + \frac{k}{\delta}[(V_w\cdot n)n + V_c - (V_c\cdot n)n]}{1 + \frac{k}{\delta}},$$ (15)

where

$$k = \lambda\left(\frac{2 - \alpha_v}{\alpha_v}\right).$$ (16)

Temperature jump is defined as

$$T_w - T_g = 2\left(\frac{2 - \alpha_T}{\alpha_T}\right)\text{Kn}L_c\frac{\partial T}{\partial n} \approx 2\left(\frac{2 - \alpha_T}{\alpha_T}\right)\frac{\lambda}{\delta}(T_g - T_c),$$ (17)

or, equivalently,

$$T_g = \frac{T_w + \beta T_c}{1 + \beta},$$ (18)

where

$$\beta = \frac{2(2 - \alpha_T)\lambda}{\alpha_T\delta}.$$ (19)

α_T is the thermal accommodation coefficient of the gas.

3.3. Solution Setup

Pressure–velocity coupling has been performed with a coupled scheme. The gradients were discretised with least square cell-based method, and pressure was calculated using a second-order equation. Density, momentum, and energy equations were undertaken using the second-order upwind scheme. Also, QUICK and MUSCL were tested for momentum equation, but no difference was observed except for 20–30% longer calculation times. The solution procedure was solved using pseudo time method, where global time step was used. For more information, refer to [44].

3.4. Grid Convergence Study

A grid convergence study (GCS) was performed on meshes M1, M2, and M3 using local and global results. A well-known approach has been adopted [46,47] based on the Richardson extrapolation method. In local analysis, the calculated variables, such as velocity magnitude, pressure, temperature, and density, were averaged at four different locations (lines). On the other hand, in global analysis, the maximum Mach number in the domain was selected as a representative integral variable.

In [46,47], it is suggested that for local analysis, a cell size Δx is defined as a representative grid size $h = \Delta x$. However, when analysing global integral quantities for three-dimensional calculations, a representative grid size is defined as

$$h = \left[\frac{1}{N} \sum_{i=1}^{N} (\Delta V_i) \right]^{1/3}, \tag{20}$$

where ΔV_i is the volume of i-th cell, and N is the total number of cells used for the computations. We constructed meshes with grid refinement factor $r = h_3/h_1$ larger than 1.3, recommended by Roache [46,47]. For meshes where $r_{21} = h_2/h_1$ and $r_{32} = h_3/h_2$ are not constant ($r_{21} \neq r_{32}$), order of convergence is defined using the following expressions:

$$p = \frac{\left| \ln \left| \frac{\epsilon_{32}}{\epsilon_{21}} \right| + q(p) \right|}{\ln(r_{21})}, \tag{21}$$

$$q(p) = \ln \left(\frac{r_{21}^p - s}{r_{32}^p - s} \right), \tag{22}$$

$$s = \frac{\epsilon_{32}/\epsilon_{21}}{|\epsilon_{32}/\epsilon_{21}|}, \tag{23}$$

where $\epsilon_{32} = \Phi_3 - \Phi_2$, $\epsilon_{21} = \Phi_2 - \Phi_1$, and Φ_k denotes the solution on the k-th grid. As one can see, Equations (21) and (22) should be solved iteratively. Note that for $r_{21} = r_{32} = \text{const}$, $q(p) = 0$; thus, there is no need for iterative calculations. The extrapolated value Φ_{ext}^{21} is then calculated as

$$\Phi_{ext}^{21} = \frac{r_{21}^p \Phi_1 - \Phi_2}{r_{21}^p - 1}. \tag{24}$$

Similarly, Φ_{ext}^{32} can be calculated as well. Two different errors are present: approximate relative error e_a^{21} and extrapolated relative error e_{ext}^{21}, respectively:

$$e_a^{21} = \left| \frac{\Phi_1 - \Phi_2}{\Phi_1} \right|, \tag{25}$$

$$e_{ext}^{21} = \left| \frac{\Phi_{ext}^{21} - \Phi_1}{\Phi_{ext}^{21}} \right|. \tag{26}$$

Finally, the fine-grid convergence index is defined as follows:

$$\text{GCI}^{21} = \frac{F_S \, e_a^{21}}{r_{21}^p - 1}, \tag{27}$$

where the security factor F_S equals 1.25 for three meshes or more, as suggested by Roache [46]. GCI^{32} and e_a^{32} are calculated analogously.

The results of the GCS (Table 2 and Figure 2) show that both GCI^{32} and GCI^{21} are low enough (<1%) that even the coarse mesh M3 provides a well-resolved solution. This indicates that the results are mesh-independent across all generated meshes. with no significant differences observed in the local grid convergence study (Appendix A).

Table 2. Global grid convergence analysis.

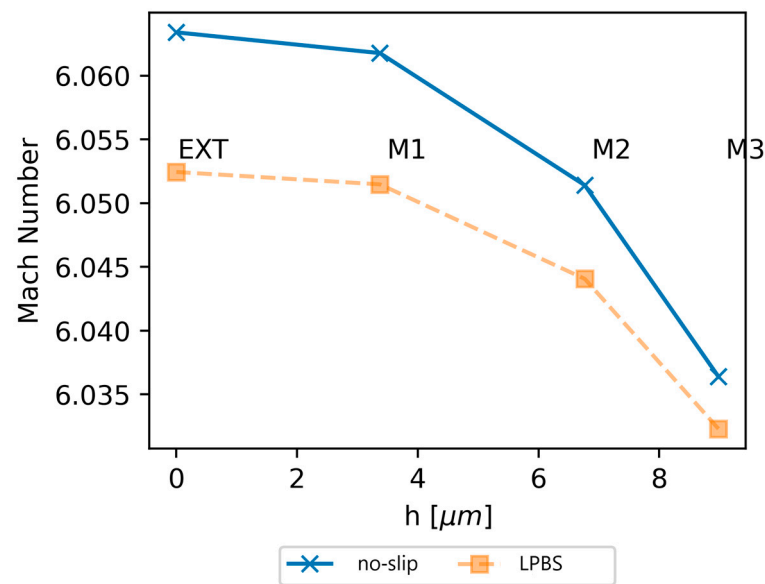| Case	Φ and Location	r_{21}	r_{32}	Φ_1	Φ_2	Φ_3	p	Φ_{ext}^{21}	e_a^{21} [%]	e_{ext}^{21} [%]	GCI^{32} [%]	GCI^{21} [%]
no-slip	Global max. Ma	2.01	1.33	6.062	6.051	6.036	2.87	6.063	0.17	0.027	0.38	0.03
LPBS	Global max. Ma	2.01	1.33	6.051	6.044	6.032	3.10	6.052	0.12	0.016	0.26	0.02

Figure 2. Grid convergence results for the case with no-slip and LPBS boundary condition. M3, M2 and M1 represent coarse, medium and fine grid, respectively. With EXT, we label extrapolated values.

No major differences were found between LPBS and no-slip boundary, with the maximum Mach number varying by less than 0.2% for all three meshes and extrapolated values. Similarly, variables analysed in the local GCS match within significantly less than 1% at most locations. Also, the GCI^{32} and GCI^{21} are significantly lower than 1% globally and, in most cases, locally. Thus, the LPBS boundary condition does not significantly affect the solution; therefore, no-slip boundary condition can be used in the CFD of sample delivery systems in SFX.

4. Results and Discussion

Numerical simulations using M2 and M3 meshes were performed on a desktop computer AMD Ryzen 9 7950X 16-Core Processor 4.50 GHz (Advanced Micro Devices, Inc., Santa Clara, CA, USA). Four cores were used for M3 and six for M2 mesh size. Calculations with M1 mesh were performed on multiprocessor server Supermicro SuperServer SYS-241E-TNRTTP (Super Micro Computer, Inc., San Jose, CA, USA) with 4× Intel Xeon Gold 6448H processors (Intel Corporation, Santa Clara, CA, USA), with a total of 132 cores, although only four cores were used for these calculations. Computational time (in core hours), the number of iterations and residuals criteria are listed in Table 1.

4.1. Flow Field Variables

The grid convergence study shows minimal differences in spatial discretisation and boundary types, so the results are presented only for M2 and no-slip boundary conditions. Figure 3 illustrates the converged solution for pressure, velocity, temperature, and density. For clarity, velocity vectors of only every 16th node are shown in Figure 3b. When the gas from two oblique capillaries (one is across the symmetry ZY plane) collides in a common point, the gas flow expands radially. The helium jet expands after exiting the nozzle to the vacuum chamber, causing the temperature to drop, as shown in Figure 3c. Due to the low pressure in the vacuum chamber, the helium density significantly decreases (Figure 3d).
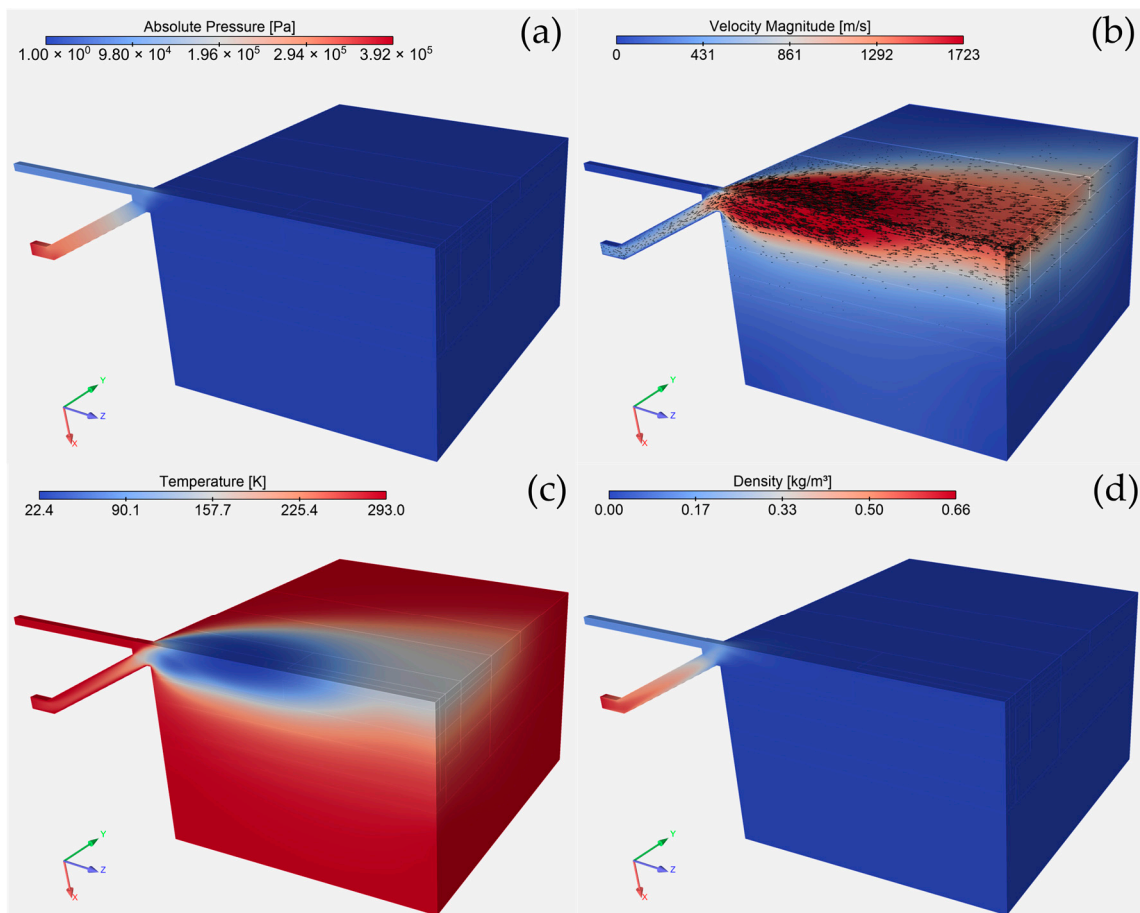
Figure 3. Flow field variables: (**a**) absolute pressure; (**b**) velocity magnitude and velocity vectors; (**c**) temperature; (**d**) density.

4.2. Dimensionless Numbers

Figure 4a,b show the cell Reynolds number and Mach number, respectively. The helium flow through the nozzle is laminar and hypersonic in the vacuum chamber.
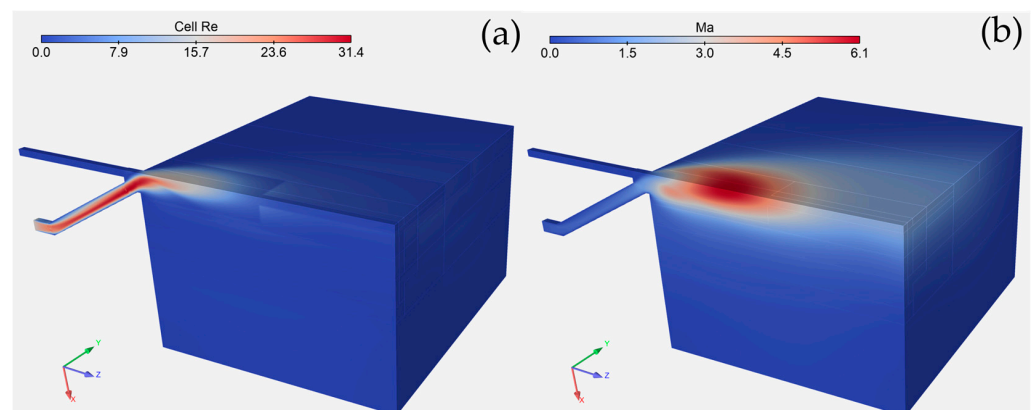

Figure 4. Dimensionless numbers: (**a**) cell Reynolds number; (**b**) Mach number.

4.3. Definition of Numerical Knudsen Number

As explained in Section 2.1, we propose Equation (8) to determine the numerical Knudsen number. Figure 5a shows the numerical Knudsen number, calculated by Equation (8), whose high values are removed in Figure 5b for clarity. Figure 5c,d shows the numerical Knudsen number calculated by Equation (6), proposed in [29]. It can be seen (Figure 5a,c) that

Equation (8) calculates ∼2 times lower Knudsen numbers inside the nozzle and for an-order-of-magnitude-lower Knudsen numbers in a vacuum chamber compared to Equation (6). The reason is that Kn_n in Equation (6) converges to the higher value between Kn_c and Kn_p, representing the maximum rather than the minimum. Also, in Figure 5d, the region with the higher Knudsen number is greater than in Figure 5b, both in nozzle and vacuum chamber, confirming that Equation (6) calculates the maximum and is unsuitable for the softmin function. Therefore, we propose Equation (8) to address the softmin function accurately.
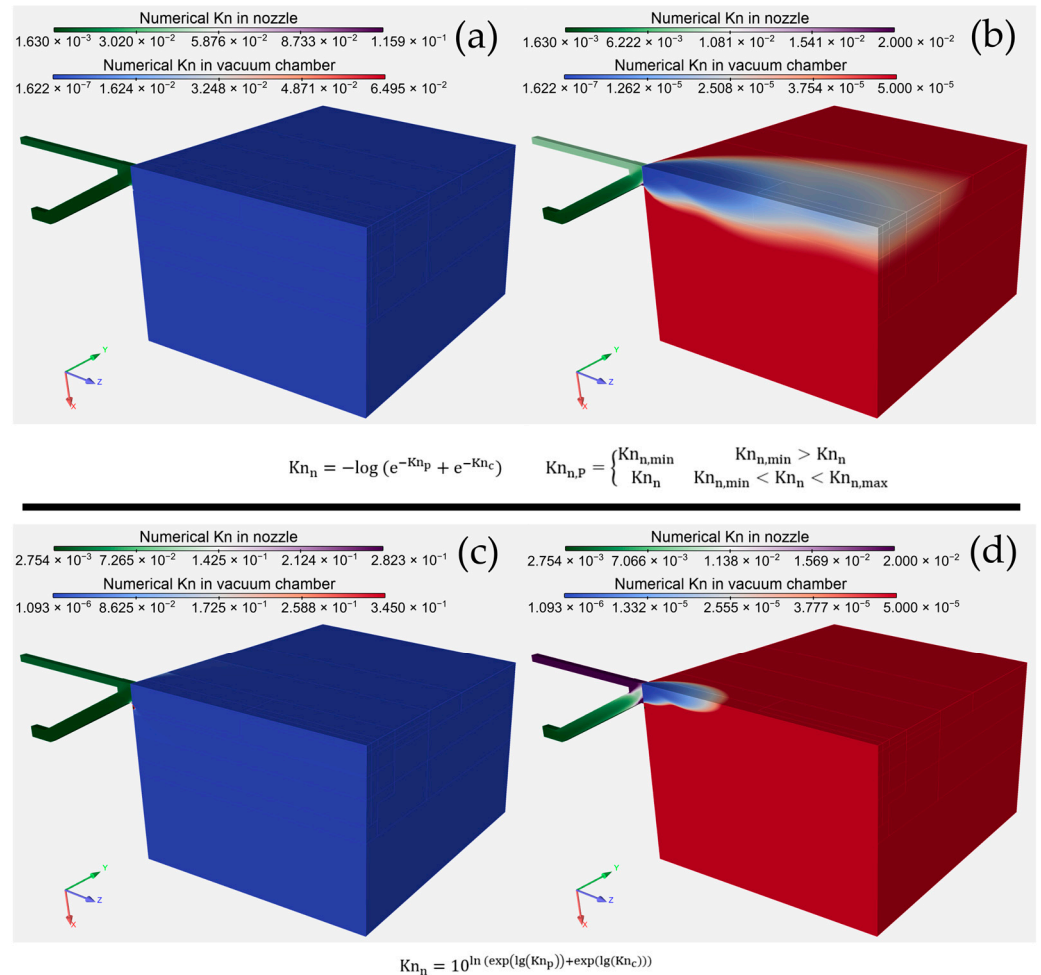

$$Kn_n = -\log\left(e^{-Kn_p} + e^{-Kn_c}\right) \qquad Kn_{n,P} = \begin{cases} Kn_{n,min} & Kn_{n,min} > Kn_n \\ Kn_n & Kn_{n,min} < Kn_n < Kn_{n,max} \end{cases}$$

$$Kn_n = 10^{\ln\left(\exp(\lg(Kn_p)) + \exp(\lg(Kn_c))\right)}$$

Figure 5. Numerical Knudsen number: (**a**) numerical Knudsen number calculated by Equation (8); (**b**) numerical Knudsen number calculated by Equation (8) with rescaled values; (**c**) numerical Knudsen number calculated by Equation (6); (**d**) numerical Knudsen number calculated by Equation (6) with rescaled values.

4.4. Knudsen Number Calculation

We calculated the mean free path λ of helium flow within each control volume using Equation (2). The cell Knudsen number is defined with the cell size $\Delta x = V_{cell}^{1/3}$, representing characteristic length. We assume that helium first flows through the nozzle and later exits the nozzle into the vacuum chamber, whose characteristic length is significantly larger than the nozzle's length. Therefore, we had to calculate the physical Knudsen number for the nozzle and vacuum chamber separately, and the calculation was undertaken using Equation (8). The expressions for Knudsen Number calculations in ANSYS Fluent are provided in the Supplementary Materials.

The characteristic length of the nozzle was assumed to be equal to the capillary diameter $L = 30$ μm. The characteristic length of the vacuum chamber diameter was set at $L \approx 300$ mm to be comparable to the experimental setup in [48].

Figure 6a shows the cell Knudsen number, Figure 6b shows the physical Knudsen number, and Figure 6d show the numerical Knudsen number. As seen in the zoomed-in areas of Figure 6b,d, the regions with the transition in the cell level and on the contact between the vacuum chamber and the nozzle exhibit high physical Knudsen values. This is due to high-pressure gradients, which influence the mean free paths.
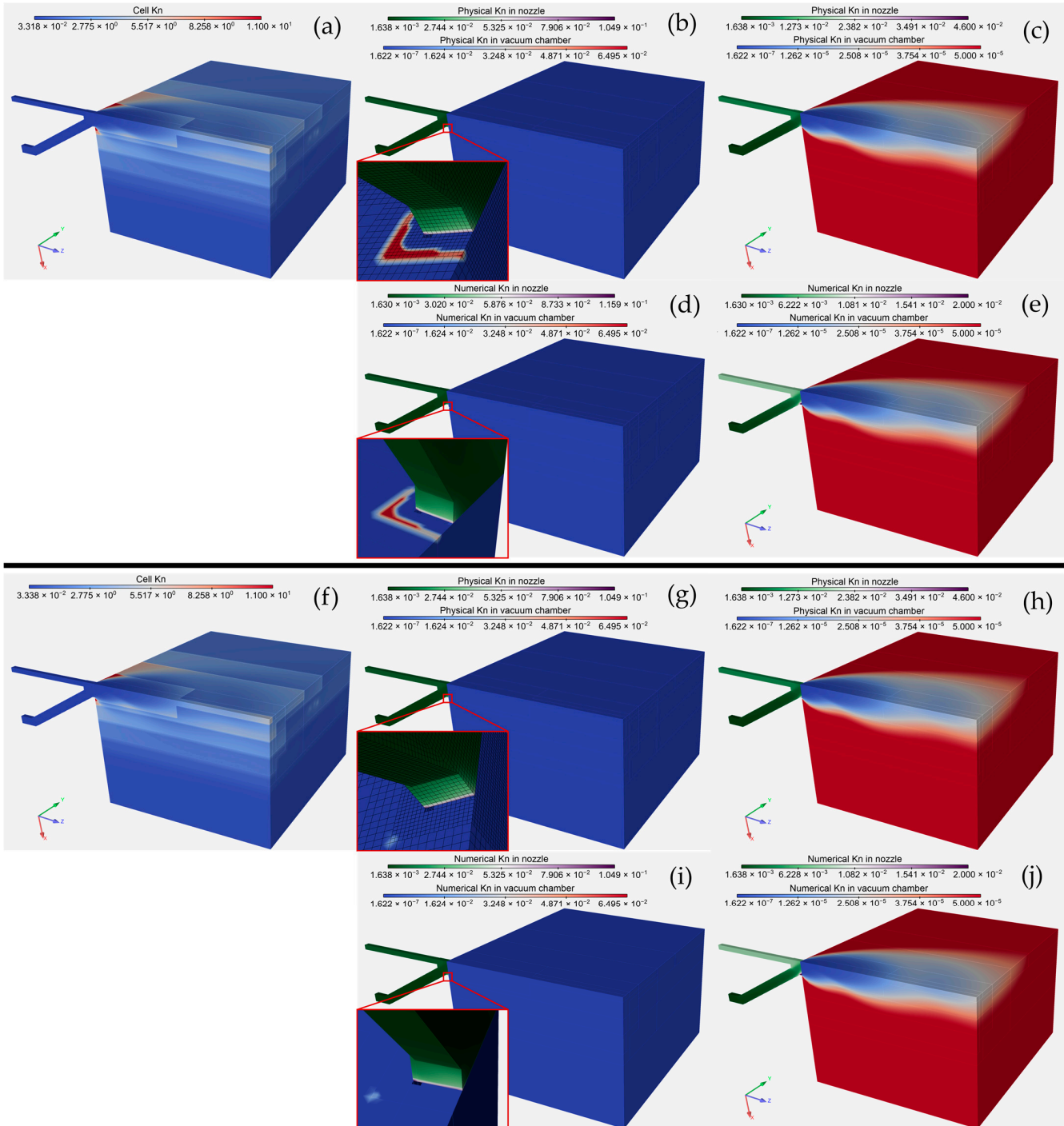

Figure 6. Knudsen number for no-slip boundary conditions: (**a**) cell Knudsen number; (**b**) physical Knudsen number; (**c**) physical Knudsen number with rescaled values; (**d**) numerical Knudsen number; (**e**) numerical Knudsen number with rescaled values. Knudsen number for LPBS boundary conditions: (**f**) cell Knudsen number; (**g**) physical Knudsen number; (**h**) physical Knudsen number with rescaled values; (**i**) numerical Knudsen number; (**j**) numerical Knudsen number with rescaled values.

These high physical Knudsen values, which were removed in Figure 6c,e, have no significant influence on the solution since the core of the expanded helium jet is relatively far away. High gradients in these regions can be tackled with a denser mesh.

The range of numerical Knudsen numbers in the nozzle is $(1.63 \times 10^{-3}, 1.16 \times 10^{-1})$, and in the vacuum chamber, $(1.62 \times 10^{-7}, 6.50 \times 10^{-2})$. The upper limit of the Knudsen number inside the nozzle is slightly out of the slip flow regime, e.g., at the start of the transitional regime, and in the vacuum chamber in the slip regime. However, these values are calculated only in a few cells at the edge of the nozzle outlet, representing less than 0.5% of the fluid domain.

Therefore, helium flow is mostly in the continuum regime, except for a small portion of the nozzle and the cells with high-pressure gradients, where flow falls in the slip regime $Kn_n > 0.01$, which requires the use of LPBS. However, since most cells are in the continuum regime, LPBS has little effect on the solution. The same conclusions apply to the physical Knudsen number. The cell Knudsen number mostly falls in the slip regime, except in the areas with high gradients, where it exceeds this range due to fine cells. In the case of M1, the cell Knudsen number is r_{21} times higher than in M2, while in M3, it is r_{32} lower than for M2.

Figure 6f–j demonstrate that the Knudsen numbers for LPBS boundary conditions show no significant differences compared to the setup with no-slip boundary conditions. The main difference is observed in the regions with high-pressure gradients, where using LPBS boundary conditions leads to lower Knudsen values (Figure 6g,h). However, both setups—using no-slip and LPBS boundary conditions—provide similar solutions, mostly within the continuum flow regime.

5. Conclusions

This work is the first detailed study of Knudsen number analysis in a sample delivery system used in SFX experiments under vacuum conditions. In simulations, most cells of the fluid domain have physical and numerical Knudsen numbers below the continuum limit (Kn < 0.01). Therefore, the CFD approach to solving Navier–Stokes equations is justified in the setup discussed here.

A few cells fall in the slip regime; therefore, the simulation with LPBS boundary conditions was tested. No significant differences were observed compared to the no-slip boundary condition. Furthermore, this is valid for all three generated meshes, namely, M1, M2, and M3, respectively, where the numerical solution is mesh-independent, as shown in local and global GCS.

In CFD, cell and physical Knudsen numbers control the numerical Knudsen number. We propose an improved equation (Equation (8)) to determine the numerical Knudsen number, which is based not only on the softmin and the sum-log-exp function; it also respects the physical meaning of those functions, meaning that the numerical Knudsen number is limited with min(Kn_c and Kn_p) and max(Kn_c and Kn_p), respectively.

We recommend applying this procedure to assess Knudsen numbers in various nozzle geometries beyond gas-focused liquid sheet designs in future work. The same Knudsen number evaluation approach may also be helpful for two-phase flow calculations, particularly for liquid sheets with sub-micron thicknesses approaching the continuum limit of the liquid phase.

Data Availability Statement: All the data generated or analysed during this study are included in this article.

Conflicts of Interest: No potential conflict of interest was reported by the authors.

Appendix A

In Table A1, the results of a local grid independence study are presented. Variables Φ were average across locations (lines) defined by two points, as follows: Line 1: $(0, 0, -1 \times 10^{-5})$ and $(1 \times 10^{-4}, 0, -1 \times 10^{-5})$; Line 2: $(0, 0, 1 \times 10^{-4})$ and $(1 \times 10^{-3}, 0, 1 \times 10^{-4})$; Line 3: $(0, 0, 1 \times 10^{-4})$ and $(0, 1 \times 10^{-3}, 1 \times 10^{-4})$; and Line 4: $(0, 0, -5 \times 10^{-5})$ and $(0, 0, 1 \times 10^{-3})$. All points coordinates are in meters.

Table A1. Local grid convergence analysis.

Φ	Location	Case	Φ_1	Φ_2	Φ_3	p	Φ_{ext}^{21}	e_a^{21} [%]	e_{ext}^{21} [%]	GCI^{32} [%]	GCI^{21} [%]
p [Pa]	Line 1	No-slip	69,625	68,950	68,985	5.283	69,638	0.0676	0.0189	0.0958	0.0237
p [Pa]	Line 1	LPBS	68,561	68,282	68,237	11.07	68,561	0.00438	0.000189	0.00554	0.000237
p [Pa]	Line 2	No-slip	11.66	8.713	5.586	0.9655	13.98	6.353	16.56	24.51	24.8
p [Pa]	Line 2	LPBS	9.867	8.009	4.18	4.467	9.955	2.332	0.8839	3.484	1.115
p [Pa]	Line 3	No-slip	50.17	47.75	48.35	0.5471	54.54	1.484	8.008	9.323	10.88
p [Pa]	Line 3	LPBS	47.88	47.79	47.79	0.4967	44.78	0.9932	6.914	6.807	8.084
p [Pa]	Line 4	No-slip	10,654	10,598	10,576	4.809	10,655	0.0435	0.0145	0.0634	0.0182
p [Pa]	Line 4	LPBS	10,524	10,501	10,476	12.05	10,524	0.00162	5.23×10^{-5}	0.00204	6.54×10^{-5}
ρ [kg m^{-3}]	Line 1	No-slip	0.1758	0.1735	0.1729	2.894	0.1761	0.1931	0.1484	0.3495	0.1858
ρ [kg m^{-3}]	Line 1	LPBS	0.1739	0.1726	0.1714	2.786	0.1742	0.1622	0.1318	0.2996	0.165
ρ [kg m^{-3}]	Line 2	No-slip	0.00341	0.00339	0.00338	0.8286	0.00343	0.1445	0.5338	0.6329	0.6709
ρ [kg m^{-3}]	Line 2	LPBS	0.00341	0.00339	0.00338	1.154	0.00342	0.1258	0.3184	0.4206	0.3992
ρ [kg m^{-3}]	Line 3	No-slip	0.00393	0.0039	0.00389	2.419	0.00393	0.1174	0.1166	0.2348	0.1459
ρ [kg m^{-3}]	Line 3	LPBS	0.00392	0.0039	0.00389	6.421	0.00392	0.0289	0.00541	0.039	0.00676
ρ [kg m^{-3}]	Line 4	No-slip	0.0288	0.0286	0.0284	2.341	0.0289	0.1486	0.1544	0.3031	0.1933
ρ [kg m^{-3}]	Line 4	LPBS	0.0285	0.0284	0.0282	2.323	0.0286	0.1299	0.1364	0.2661	0.1707
T [K]	Line 1	No-slip	198.72	199.47	200.3	0.602	197.6	0.1068	0.5678	0.6161	0.7057
T [K]	Line 1	LPBS	197.71	198.45	199.64	0.3577	195.08	0.1444	1.35	1.337	1.666
T [K]	Line 2	No-slip	242.49	242.2	241.53	2.806	242.54	0.0237	0.0191	0.0435	0.0238
T [K]	Line 2	LPBS	242.2	241.9	241.19	6.431	242.2	0.00786	0.00147	0.0106	0.00183
T [K]	Line 3	No-slip	234.06	234.09	234.19	2.04	234.09	0.0104	0.013	0.0231	0.0163
T [K]	Line 3	LPBS	233.83	233.91	234.01	1.819	233.95	0.037	0.0538	0.0886	0.0673
T [K]	Line 4	No-slip	101.62	102.21	102.29	2.183	101.5	0.101	0.1157	0.2149	0.1445
T [K]	Line 4	LPBS	101.66	102.11	102.37	1.144	101.28	0.1441	0.3711	0.4853	0.4622

Table A1. *Cont.*

Φ	Location	Case	Φ_1	Φ_2	Φ_3	p	Φ_{ext}^{21}	e_a^{21} [%]	e_{ext}^{21} [%]	GCI^{32} [%]	GCI^{21} [%]
v [m s^{-1}]	Line 1	No-slip	934.6	937.77	935.24	2.639	934.07	0.0649	0.0571	0.1234	0.0714
v [m s^{-1}]	Line 1	LPBS	940.35	942.5	938.02	11.37	940.35	0.00218	8.58×10^{-5}	0.00275	0.000107
v [m s^{-1}]	Line 2	No-slip	482.16	488.5	495.98	2.676	481.19	0.2346	0.2028	0.4429	0.2529
v [m s^{-1}]	Line 2	LPBS	482.75	488.21	496.85	3.485	482.22	0.1913	0.111	0.3161	0.1386
v [m s^{-1}]	Line 3	No-slip	513.05	515.37	514.89	0.7127	510.35	0.12	0.5301	0.5977	0.6591
v [m s^{-1}]	Line 3	LPBS	515	515.28	515.6	1.248	512.25	0.2304	0.5364	0.7253	0.667
v [m s^{-1}]	Line 4	No-slip	1426.3	1430.6	1432.6	1.087	1424	0.0604	0.1649	0.2119	0.2058
v [m s^{-1}]	Line 4	LPBS	1426.3	1428.7	1432.3	1.108	1424.2	0.0549	0.1464	0.1896	0.1828

References

1. Chapman, H.N.; Fromme, P.; Barty, A.; White, T.A.; Kirian, R.A.; Aquila, A.; Hunter, M.S.; Schulz, J.; DePonte, D.P.; Weierstall, U. Femtosecond X-ray Protein Nanocrystallography. *Nature* **2011**, *470*, 73–77. [CrossRef] [PubMed]
2. Gañán-Calvo, A.M. Generation of Steady Liquid Microthreads and Micron-Sized Monodisperse Sprays in Gas Streams. *Phys. Rev. Lett.* **1998**, *80*, 285–288. [CrossRef]
3. DePonte, D.P.; Weierstall, U.; Schmidt, K.; Warner, J.; Starodub, D.; Spence, J.C.H.; Doak, R.B. Gas Dynamic Virtual Nozzle for Generation of Microscopic Droplet Streams. *J. Phys. D Appl. Phys.* **2008**, *41*, 195505. [CrossRef]
4. Beyerlein, K.R.; Adriano, L.; Heymann, M.; Kirian, R.; Knoška, J.; Wilde, F.; Chapman, H.N.; Bajt, S. Ceramic Micro-Injection Molded Nozzles for Serial Femtosecond Crystallography Sample Delivery. *Rev. Sci. Instrum.* **2015**, *86*, 125104. [CrossRef] [PubMed]
5. Weierstall, U. Liquid Sample Delivery Techniques for Serial Femtosecond Crystallography. *Philos. Trans. R. Soc. B Biol. Sci.* **2014**, *369*, 20130337. [CrossRef] [PubMed]
6. Schulz, J.; Bielecki, J.; Doak, R.B.; Dörner, K.; Graceffa, R.; Shoeman, R.L.; Sikorski, M.; Thute, P.; Westphal, D.; Mancuso, A.P. A Versatile Liquid-Jet Setup for the European XFEL. *J. Synchrotron Radiat.* **2019**, *26*, 339–345. [CrossRef]
7. Kondoh, M.; Tsubouchi, M. Liquid-Sheet Jets for Terahertz Spectroscopy. *Opt. Express* **2014**, *22*, 14135. [CrossRef]
8. Ekimova, M.; Quevedo, W.; Faube, M.; Wernet, P.; Nibbering, E.T.J. A Liquid Flatjet System for Solution Phase Soft-X-ray Spectroscopy. *Struct. Dyn.* **2015**, *2*, 054301. [CrossRef]
9. Galinis, G.; Strucka, J.; Barnard, J.C.T.; Braun, A.; Smith, R.A.; Marangos, J.P. Micrometer-Thickness Liquid Sheet Jets Flowing in Vacuum. *Rev. Sci. Instrum.* **2017**, *88*, 083117. [CrossRef]
10. Barnard, J.C.T.; Lee, J.P.; Alexander, O.; Jarosch, S.; Garratt, D.; Picciuto, R.; Kowalczyk, K.; Ferchaud, C.; Gregory, A.; Matthews, M.; et al. Delivery of Stable Ultra-Thin Liquid Sheets in Vacuum for Biochemical Spectroscopy. *Front. Mol. Biosci.* **2022**, *9*, 1044610. [CrossRef]
11. Buchmann, A.; Hoberg, C.; Havenith, M. Improvements in Windowless Spectroscopy: 3D Printed Nozzles. In Proceedings of the International Conference on Infrared, Millimeter, and Terahertz Waves, IRMMW-THz, Delft, The Netherlands, 28 August–2 September 2022.
12. Yin, Z.; Luu, T.T.; Wörner, H.J. Few-Cycle High-Harmonic Generation in Liquids: In-Operando Thickness Measurement of Flat Microjets. *J. Phys. Photon.* **2020**, *2*, 044007. [CrossRef]
13. Hoffman, D.J.; van Driel, T.B.; Kroll, T.; Crissman, C.J.; Ryland, E.S.; Nelson, K.J.; Cordones, A.A.; Koralek, J.D.; DePonte, D.P. Microfluidic Liquid Sheets as Large-Area Targets for High Repetition XFELs. *Front. Mol. Biosci.* **2022**, *9*, 1048932. [CrossRef] [PubMed]
14. Chang, Y.P.; Yin, Z.; Balciunas, T.; Wörner, H.J.; Wolf, J.P. Temperature Measurements of Liquid Flat Jets in Vacuum. *Struct. Dyn.* **2022**, *9*, 014901. [CrossRef] [PubMed]
15. Fondell, M.; Eckert, S.; Jay, R.M.; Weniger, C.; Quevedo, W.; Niskanen, J.; Kennedy, B.; Sorgenfrei, F.; Schick, D.; Giangrisostomi, E.; et al. Time-Resolved Soft X-ray Absorption Spectroscopy in Transmission Mode on Liquids at MHz Repetition Rates. *Struct. Dyn.* **2017**, *4*, 054902. [CrossRef] [PubMed]
16. George, K.M.; Morrison, J.T.; Feister, S.; Ngirmang, G.K.; Smith, J.R.; Klim, A.J.; Snyder, J.; Austin, D.; Erbsen, W.; Frische, K.D.; et al. High-Repetition-Rate (KHz) Targets and Optics from Liquid Microjets for High-Intensity Laser–Plasma Interactions. *High Power Laser Sci. Eng.* **2019**, *7*, e50. [CrossRef]
17. Luu, T.T.; Yin, Z.; Jain, A.; Gaumnitz, T.; Pertot, Y.; Ma, J.; Wörner, H.J. Extreme–Ultraviolet High–Harmonic Generation in Liquids. *Nat. Commun.* **2018**, *9*, 3723. [CrossRef]
18. Smith, A.D.; Balčiu Nas, T.; Chang, Y.-P.; Schmidt, C.; Zinchenko, K.; Nunes, F.B.; Rossi, E.; Svoboda, V.; Yin, Z.; Wolf, J.-P.; et al. Femtosecond Soft-X-ray Absorption Spectroscopy of Liquids with a Water-Window High-Harmonic Source. *J. Phys. Chem. Lett.* **2020**, *11*, 1981–1988. [CrossRef]
19. Koralek, J.D.; Kim, J.B.; Brůža, P.; Curry, C.B.; Chen, Z.; Bechtel, H.A.; Cordones, A.A.; Sperling, P.; Toleikis, S.; Kern, J.F.; et al. Generation and Characterization of Ultrathin Free-Flowing Liquid Sheets. *Nat. Commun.* **2018**, *9*, 1353. [CrossRef]

20. Konold, P.E.; You, T.; Bielecki, J.; Valerio, J.; Kloos, M.; Westphal, D.; Bellisario, A.; Varma Yenupuri, T.; Wollter, A.; Koliyadu, J.C.P.; et al. 3D-Printed Sheet Jet for Stable Megahertz Liquid Sample Delivery at X-Ray Free-Electron Lasers. *IUCrJ* **2023**, *10*, 662–670. [CrossRef]

21. Yang, J.; Nunes, J.P.F.; Ledbetter, K.; Biasin, E.; Centurion, M.; Chen, Z.; Cordones, A.A.; Crissman, C.; Deponte, D.P.; Glenzer, S.H.; et al. Structure Retrieval in Liquid-Phase Electron Scattering. *Phys. Chem. Chem. Phys.* **2021**, *23*, 1308–1316. [CrossRef]

22. Nunes, J.P.F.; Ledbetter, K.; Lin, M.; Kozina, M.; DePonte, D.P.; Biasin, E.; Centurion, M.; Crissman, C.J.; Dunning, M.; Guillet, S.; et al. Liquid-Phase Mega-Electron-Volt Ultrafast Electron Diffraction. *Struct. Dyn.* **2020**, *7*, 024301. [CrossRef] [PubMed]

23. Šarler, B.; Zahoor, R.; Bajt, S. Alternative Geometric Arrangements of the Nozzle Outlet Orifice for Liquid Micro-Jet Focusing in Gas Dynamic Virtual Nozzles. *Materials* **2021**, *14*, 1572. [CrossRef] [PubMed]

24. Zahoor, R.; Bajt, S.; Šarler, B. Influence of Gas Dynamic Virtual Nozzle Geometry on Micro-Jet Characteristics. *Int. J. Multiph. Flow* **2018**, *104*, 152–165. [CrossRef]

25. Zahoor, R.; Belšak, G.; Bajt, S.; Šarler, B. Simulation of Liquid Micro-Jet in Free Expanding High-Speed Co-Flowing Gas Streams. *Microfluid. Nanofluidics* **2018**, *22*, 87. [CrossRef]

26. Zahoor, R.; Bajt, S.; Šarler, B. Simulation of Non-Newtonian Gas-Focused Micro-Jets in Chocked Gas Flow Regime. *J. Phys. Conf. Ser.* **2024**, *2766*, 012069. [CrossRef]

27. Belšak, G.; Bajt, S.; Šarler, B. Computational Modeling and Simulation of Gas Focused Liquid Micro-Sheets. *Int. J. Multiph. Flow* **2021**, *140*, 103666. [CrossRef]

28. Chambre, P.A.; Schaaf, S.A. *Flow of Rarefied Gases*; Princeton University Press: Princeton, NJ, USA, 1961; ISBN 9781400885800.

29. Liu, C.; Zhou, G.; Shyy, W.; Xu, K. Limitation Principle for Computational Fluid Dynamics. *Shock. Waves* **2019**, *29*, 1083–1102. [CrossRef]

30. Liu, C.; Xu, K.; Zhou, G. Cell Size Effect on Computational Fluid Dynamics: The Limitation Principle for Flow Simulation. *arXiv* **2018**, arXiv:1706.08200.

31. Ghorbel, M.; Pineau, J.; Gourdeau, R.; Javdani, S.; Srinivasa, S. A Decision-Theoretic Approach for the Collaborative Control of a Smart Wheelchair. *Int. J. Soc. Robot.* **2018**, *10*, 131–145. [CrossRef]

32. Sengupta, T.K.; Sengupta, A.; Sharma, N.; Sengupta, S.; Bhole, A.; Shruti, K.S. Roles of Bulk Viscosity on Rayleigh-Taylor Instability: Non-Equilibrium Thermodynamics Due to Spatio-Temporal Pressure Fronts. *Phys. Fluids* **2016**, *28*, 094102. [CrossRef]

33. Chen, S.; Wang, X.; Wang, J.; Wan, M.; Li, H.; Chen, S. Effects of Bulk Viscosity on Compressible Homogeneous Turbulence. *Phys. Fluids* **2019**, *31*, 085115. [CrossRef]

34. Lin, J.; Scalo, C.; Hesselink, L. Bulk Viscosity Model for Near-Equilibrium Acoustic Wave Attenuation. *arXiv* **2017**, arXiv:1707.05876.

35. Buresti, G. A Note on Stokes' Hypothesis. *Acta Mech.* **2015**, *226*, 3555–3559. [CrossRef]

36. Sharma, B.; Kumar, R. Estimation of Bulk Viscosity of Dilute Gases Using a Nonequilibrium Molecular Dynamics Approach. *Phys. Rev. E* **2019**, *100*, 013309. [CrossRef] [PubMed]

37. Pan, X.; Shneider, M.N.; Miles, R.B. Coherent Rayleigh-Brillouin Scattering in Molecular Gases. *Phys. Rev. A* **2004**, *69*, 033814. [CrossRef]

38. Pan, S.; Johnsen, E. The Role of Bulk Viscosity on the Decay of Compressible, Homogeneous, Isotropic Turbulence. *J. Fluid. Mech.* **2017**, *833*, 717–744. [CrossRef]

39. Boukharfane, R.; Ferrer, P.J.M.; Mura, A.; Giovangigli, V. On the Role of Bulk Viscosity in Compressible Reactive Shear Layer Developments. *Eur. J. Mech. B/Fluids* **2019**, *77*, 32–47. [CrossRef]

40. Prangsma, G.J.; Alberga, A.H.; Beenakker, J.J.M. Ultrasonic Determination of the Volume Viscosity of N_2, CO, CH_4 and CD_4 between 77 and 300 K. *Physica* **1973**, *64*, 278–288. [CrossRef]

41. Emanuel, G. Bulk Viscosity of a Dilute Polyatomic Gas. *Phys. Fluids A Fluid. Dyn.* **1990**, *2*, 2252–2254. [CrossRef]

42. Tisza, L. Supersonic Absorption and Stokes' Viscosity Relation. *Phys. Rev.* **1942**, *61*, 531–536. [CrossRef]

43. Kim, Y.J.; Kim, Y.-J.; Han, J.-G. Numerical Analysis of Flow Characteristics of an Atmospheric Plasma Torch. *arXiv* **2004**, arXiv:physics/0410237.

44. ANSYS. *ANSYS Fluent Theory Guide 2021R1*; ANSYS, Inc.: Canonsburg, PA, USA, 2021.

45. Matteucci, S.; Yampolskii, Y.; Freeman, B.D.; Pinnau, I. Transport of Gases and Vapors in Glassy and Rubbery Polymers. In *Materials Science of Membranes for Gas and Vapor Separation*; Wiley: Hoboken, NJ, USA, 2006; pp. 1–47.

46. Roache, P.J. Quantification of Uncertainty In Computational Fluid. *Annu. Rev. Fluid. Mech.* **1997**, *29*, 123–160. [CrossRef]

47. Celik, I.B.; Ghia, U.; Roache, P.J.; Freitas, C.J.; Coleman, H.; Raad, P.E. Procedure for Estimation and Reporting of Uncertainty Due to Discretization in CFD Applications. *J. Fluids Eng.* **2008**, *130*, 078001. [CrossRef]

48. Zupan, B.; Peña-Murillo, G.E.; Zahoor, R.; Gregorc, J.; Šarler, B.; Knoška, J.; Gañán-Calvo, A.M.; Chapman, H.N.; Bajt, S. An Experimental Study of Liquid Micro-Jets Produced with a Gas Dynamic Virtual Nozzle under the Influence of an Electric Field. *Front. Mol. Biosci.* **2023**, *10*, 1006733. [CrossRef]